

Understanding the UV/Optical Variability of AGNs through Quasi-Periodic Large-scale Magnetic Dynamos

Hongzhe Zhou^{1,*}, Dong Lai^{2,1}

¹ Tsung-Dao Lee Institute, Shanghai Jiao Tong University, Shanghai, 201210, China

² Department of Astronomy and Cornell Center for Astrophysics and Planetary Science, Cornell University, Ithaca, NY 14853, USA

November 21, 2024

ABSTRACT

Context. The UV/optical light curves observed in active galactic nuclei (AGNs) are well-characterized by damped random walk (DRW) process, with the damping timescale τ_d exhibiting correlations with both the black hole mass (M_{BH}) and the photon wavelength (λ). However, the underlying physical origins for the DRW process and the scaling laws remain unclear.

Aims. We aim to understand the AGN variability induced by a quasi-periodic large-scale dynamo in an accretion disk, and examine whether it reproduces the observed variability features in AGN UV/optical light curves.

Methods. Using a one-dimensional, optically thick, geometrically thin disk model, we introduce variability into the viscosity parameter α by incorporating quasi-periodic large-scale magnetic fields. We calculate the power spectral densities (PSDs) of the accretion rates and the disk thermal emission, and fit for their damping time scales. The disk and dynamo parameters are adjusted to explore how τ_d scales with them.

Results. With reasonable dynamo parameters, our model successfully reproduces both the linear relation between the root-mean-square and the mean values of the radiation flux, and the log-normal distribution of the flux variability. The PSDs of accretion rates and radiation fluxes align well with DRW models, and yield consistent values of τ_d with AGN observations. Analytical arguments, supported by numerical evidence, suggest that the flattening of flux PSDs at low frequencies is governed by the timescale at the inner boundary of the emission region for a given wavelength. For $M_{\text{BH}} \gtrsim 10^6 M_{\odot}$, variations in the Eddington ratio flatten the τ_d - M_{BH} scaling, resulting in $\tau_d \propto M_{\text{BH}}^{0.5-1}$. For $M_{\text{BH}} \lesssim 10^6 M_{\odot}$, we find a steeper scaling, $\tau_d \propto M_{\text{BH}}$. Including further refinements, such as the dependence of dynamo properties on M_{BH} and AGN luminosity, and accounting for X-ray reprocessing, would further enhance the accuracy of the model compared to observations.

1. Introduction

Accretion flows around supermassive black holes (SMBHs) at galaxy centers provide one of the most compelling laboratories for studying plasmas under extreme physical conditions. Among the various observational signatures, the electromagnetic radiation emitted in accretion disks offers critical insights into these dynamic environments. It has long been established that the UV/optical emissions from active galactic nuclei (AGNs) exhibit stochastic variability (Uttley & McHardy 2001; Kelly et al. 2009; MacLeod et al. 2010; Burke et al. 2021; Tang et al. 2023), characterized by several peculiar features whose origins remain elusive. Since the UV/optical band coincides with the thermal emission from a thin accretion disk surrounding a SMBH, understanding its variability is crucial as it may encode vital information about the accretion disk.

We briefly review the known properties of the UV/optical variability in AGNs and some other compact systems. At some given photon wavelength λ , the fluctuating radiation flux F_{λ} typically exhibits a linear relation between its root-mean-squared (rms) and mean values, which reflects the intrinsic nonlinearity in the underlying stochastic process (Uttley & McHardy 2001; Uttley et al. 2005). The power spectral densities (PSDs) of the radiation fluxes can usually be well fitted by the damped random walk (DRW) model, which shows a -2 power-law index at high frequencies and transitions to nearly white noise at low frequencies (Kelly et al. 2009; MacLeod et al. 2010; Zu et al. 2013), although slightly steeper high-frequency slopes have also been ob-

served (Mushotzky et al. 2011). Similar DRW-like PSDs have also been identified in the sub-millimeter (Chen et al. 2023) and the X-ray bands (Zhang et al. 2024).

In the DRW model, the damping timescale τ_d is defined as the inverse of the critical frequency where the PSD slope changes. The relationship between τ_d and the mass of the SMBH (M_{BH}), rest-frame luminosity (L), accretion rate (\dot{M}) and redshift (z) has been widely studied. By observing individual quasars in different wavebands, MacLeod et al. (2010) found $\tau_d \propto \lambda^{0.17 \pm 0.02}$. Applying this relation to different AGNs, MacLeod et al. (2010) also found a rather weak dependence of τ_d on the rest-frame luminosity or the redshift. On the other hand, the scaling with M_{BH} is typically found to be stronger, with power-law indices $\lesssim 1$ and a preference for values closer to $\lesssim 0.5$ (Kelly et al. 2009; MacLeod et al. 2010; Burke et al. 2021; Wang et al. 2023; Arévalo et al. 2024).

It has been argued that short observation baselines can underestimate τ_d (Stone et al. 2022; Zhou et al. 2024; Ren et al. 2024). In particular, the true value of τ_d , rather than the measured value, must be smaller than 10% of the baseline. For this reason, the measurements by Kelly et al. (2009) and Burke et al. (2021) have been argued to be biased, particularly for the high-mass galaxies. From unbiased samples, Ren et al. (2024) find $\tau_d \propto L^{0.72} \lambda^{1.19}$, which is consistent with the corona-heated accretion-disk reprocessing (CHAR) model proposed by the same group (Sun et al. 2020; Zhou et al. 2024).

The origin of the observed DRW-like UV/optical variability and the $\tau_d(M_{\text{BH}}, \lambda)$ relation remains elusive, and observations beyond AGN systems and in other wavebands offer some

* Corresponding author; hongzhe.zhou@sjtu.edu.cn

hints. The $\tau_d \sim M_{\text{BH}}^{0.5}$ scaling has been found to apply to stellar-mass black holes, accreting white dwarfs, as well as young stellar objects (Scaringi et al. 2015; Su et al. 2024), indicating that the scaling is likely universal for accretion disks and does not have a general-relativistic origin, such as the Bardeen-Peterson effect (Bardeen & Petterson 1975; Nelson & Papaloizou 2000). Furthermore, similar scalings have been observed in the X-ray band (Zhang et al. 2024). Given that X-ray emission is often associated with AGN jet activity, this suggests that DRW-type variabilities may be closely linked to magnetic processes in accretion flows.

In fact, the idea of magnetic origin of AGN variabilities has been proposed by several authors. One possibility is the intrinsic fluctuations of turbulence driven by the magnetorotational instability (MRI; Velikhov 1959; Chandrasekhar 1961; Balbus & Hawley 1991) in the accretion disk, as discussed in King et al. (2004), Mayer & Pringle (2006), and Janiuk & Czerny (2007). It has also been demonstrated by Hogg & Reynolds (2016) using global disk simulations that turbulence in the disk naturally yields luminosity variations whose PSD is close to DRW.

To understand how turbulence fluctuations may affect accretion disk emissions, one couples the former to the disk dynamics through the viscosity parameter α (Shakura & Sunyaev 1973). A general analytical framework for studying viscosity fluctuations was considered by Lyubarskii (1997) (hereafter L97), who explored the consequences of random fluctuations in α that are correlated in time but uncorrelated in space. The L97 model was numerically solved by Cowperthwaite & Reynolds (2014) and Turner & Reynolds (2021), and indeed it exhibited a broken power law for the PSD of the light curve, a linear rms-flux relation and a log-normal distribution of the flux. However, the L97 model accounts only for the effects of prescribed α fluctuations, but lacks an underlying physical mechanism to explain what drives these fluctuations, which remains an open question.

As an alternative to an intrinsically varying disk, the UV/optical AGN variability could be driven by reprocessing variable X-rays from the inner disk (Krolik et al. 1991), as demonstrated in shearing-box simulations by Secunda et al. (2024). In the recent CHAR model proposed by Sun et al. (2020), random magnetic reconnection and flare events in the disk corona heat the disk, inducing variability in the accretion rate. By introducing a red-noise heating rate, such a model can self-consistently explain several observational features of AGN UV/optical light curves, including DRW-compatible PSDs, inter-band time lags, and the bluer-when-brighter color variability. Similar to the L97 model, the sourcing coronal variability has to be prescribed in the CHAR model, but the physical origin of the variability is not addressed.

In the present work, we propose the possibility that a quasi-periodic large-scale dynamo (LSD) in an accretion disk leads to the disk's emission variabilities. In contrast to the phenomenological L97 model, our work is rooted in the physics of accretion disk dynamos. Indeed, periodic LSDs have been routinely observed in both shearing-box and global accretion disk simulations (Gressel 2010; Bai & Stone 2013; Hogg & Reynolds 2018), in which magnetic fields are amplified from weak seed fields and resemble LSD waves whose coherent length and time scales are ~ 30 times the disk scale height and the orbital time scale, respectively. By randomly stretching the LSD fields, the MRI turbulence grows a component that also exhibits quasi-periodicity, which, as we propose, will be reflected in the variability of the turbulent viscosity and the mass accretion rate.

Our proposed fluctuating accretion model solves the one-dimensional disk diffusion equation, similar to those used in Lyubarskii (1997) and Turner & Reynolds (2021), but with greater realism by incorporating the underlying physics—namely, the LSD—as the driver of fluctuations and variabilities. By assuming that the disk Maxwell stress linearly responds to the LSD waves, we demonstrate that our model naturally produces a DRW-shape PSD for the disk thermal emission, even though the LSD waves are not presumed to follow DRW processes (cf. Dexter & Agol 2011; Cai et al. 2016). We also show that our model can explain a number of the features of the observed AGN UV/optical variabilities. If the dynamo amplified fields are advected into the inner disk to form a hot and compact corona, the reconnection between the field lines with alternative polarities also provides a natural source of variability for the reprocessing models (Hagen et al. 2024).

The rest of the paper is organized as follows. In Sec. 2 we introduce our fluctuating disk model and the governing equations. In Sec. 3 we showcase and explain the numerical results for the variabilities produced by our model. We conclude in Sec. 4.

2. Dynamo-driven fluctuating disk model and governing equations

We consider a geometrically thin, optically thick disk with a Keplerian rotation profile $\Omega(r)$. Assuming that the angular momentum transport is dominated by the turbulent viscous stress, the vertically integrated and azimuthally averaged viscous-diffusive equation of the surface density Σ is (see, e.g., Frank et al. 2002)

$$\partial_t \Sigma - \frac{3}{r} \partial_r \left[r^{1/2} \partial_r (r^{1/2} \nu \Sigma) \right] = 0, \quad (1)$$

where $\nu(t, r)$ is the turbulent viscosity with spatial and temporal variabilities. At radius r , the accretion rate is given by

$$\dot{M}(t, r) = 6\pi r^{1/2} \partial_r (r^{1/2} \nu \Sigma), \quad (2)$$

and the energy dissipation rate per unit surface area is

$$D(t, r) = \frac{1}{2} \nu \Sigma (r \partial_r \Omega)^2 = \frac{9}{8} \nu \Sigma \Omega^2. \quad (3)$$

For an optically thick disk, the radiating blackbody temperature at the disk surface is $T(t, r) = (D/\sigma_{\text{SB}})^{1/4}$, with σ_{SB} being the Stefan-Boltzmann constant. The specific flux at photon wavelength λ from a face-on disk at distance d is then

$$F_\lambda = \frac{4\pi h c^2}{d^2 \lambda^5} \int_{r_0}^{r_{\text{out}}} \frac{r dr}{e^{hc/\lambda k_B T} - 1}, \quad (4)$$

where h is the Planck constant, c is the speed of the light, k_B is the Boltzmann constant, and r_0 and r_{out} are the inner and outer radii of the disk, respectively. The total luminosity from the thermal emission is

$$L(t) = 4\pi \int_{r_0}^{r_{\text{out}}} D(t, r) r dr. \quad (5)$$

2.1. Description of turbulent viscosity

We consider a Shakura-Sunyaev type viscosity that is scaled by the local sound speed $c_s(r)$ and disk scale height $H(r)$, and the dimensionless viscosity parameter α has both spatial and temporal variations, so that

$$\nu(t, r) = \alpha(t, r) c_s(r) H(r). \quad (6)$$

For thin disks, force balance in the vertical direction gives $c_s = \Omega H$. Additionally, with Kramers' law for opacity, the dimensionless disk scale height is $\epsilon = H/r \propto r^{1/8}$ (Frank et al. 2002). Hence

$$v(t, r) = \alpha(t, r) c_{s0} H_0 \left(\frac{r}{r_0} \right)^{3/4}, \quad (7)$$

where the subscript 0 indicates quantities evaluated at the disk inner boundary $r = r_0$. In the derivation above, we have assumed that the variabilities in c_s and H are small compared to that of α in Eq. (6), justified by the relation $c_s^2 \propto T \propto \nu^{1/4} \propto \alpha^{1/4} c_s^{1/2}$, and hence the weak dependence $c_s \propto \alpha^{1/6}$.

The dimensionless viscosity parameter α is defined using the mean of the turbulent Reynolds and Maxwell stresses, i.e.,

$$\alpha = \frac{\rho (\overline{u_r u_\phi} - \overline{b_r b_\phi})}{P}, \quad (8)$$

where ρ is the gas density, P is the thermal pressure, and \mathbf{u} and \mathbf{b} are the turbulent velocity and magnetic field, respectively. The magnetic field is measured in the Alfvén unit, and the overlines indicate azimuthally averaged quantities. We model the variability of α by assuming that (i) the turbulent Maxwell stress dominates in Eq. (8), as has been routinely observed in simulations (see Blackman et al. 2008, for a summary), and (ii) the turbulent Maxwell stress has a stationary part representing a steady-state turbulence, and a variable part because of its response to a quasi-periodic LSD. Correspondingly we write

$$\alpha(t, r) = \alpha_0 [1 + \tilde{\alpha}_{\text{LSD}}(t, r)], \quad (9)$$

where α_0 is the stationary part of the viscosity parameter, and $\tilde{\alpha}_{\text{LSD}}$ is the normalized variable part. This two-component model is justified by the separation of time scales in the problem. Consider the case where the disk hosts a small-scale dynamo whose growth time scale is comparable to the Keplerian time Ω^{-1} , as well as a large-scale dynamo which has cycle periods of order $C_\Omega \Omega^{-1}$ and $C_\Omega \sim 30$ (Gressel 2010; Bai & Stone 2013; Hogg & Reynolds 2016). Since we consider the azimuthally averaged disk dynamics, the time scale of our interest is at least a few time longer than Ω^{-1} , allowing us to ignore fluctuations of α over the turbulence time scale. Meanwhile, the time scale of interest is still shorter than the large-scale dynamo time scale, and hence we need to consider the response of $\overline{b_r b_\phi}$ to the mean-field stress, which we assume to be linear in this work. The large-scale magnetic fields may additionally contribute non-local angular momentum transport (Blackman & Nauman 2015), which we do not consider in the present work. In the next subsection we detail the prescription of $\tilde{\alpha}_{\text{LSD}}$.

2.2. Prescription of dynamo waves

LSDs that amplify disk-scale magnetic fields can be realized in high-resolution simulations that resolve a sufficiently extended turbulent inertial range (Gressel 2010; Bai & Stone 2013; Hogg & Reynolds 2018; Liska et al. 2020; Dhang et al. 2020), or low-resolution simulations which incorporate sub-grid dynamo terms (von Rekowski et al. 2003; Bucciantini & Del Zanna 2013; Bugli et al. 2014; Stepanovs et al. 2014; Sądowski et al. 2015; Fendt & Gaßmann 2018; Dyda et al. 2018; Tómei et al. 2020; Vourellis & Fendt 2021; Zhou 2024). For thin disks, both local and global simulations display dipolar field configurations and radially outgoing dynamo waves. The coherent length and time scales of the fields

are both ~ 30 times larger than those of the turbulent fields. Fig. 1(a) gives an example of the space-time diagram of the LSD-amplified large-scale \overline{B}_ϕ using the data of run A01 in Zhou (2024).

We now consider a semi-analytical model of the mean magnetic field $\overline{B}_{r,\phi}(t, r)$ in the disk. Here we only consider their radial variation; in the vertical direction, both \overline{B}_r and \overline{B}_ϕ are anti-symmetric with respect to the disk mid-plane because of the dipolar geometry, leaving the stress $\overline{B}_r \overline{B}_\phi$ with a uniform sign across the mid-plane. Around radius r , we parameterize the dynamo wave's frequency ω_{LSD} and wavenumber k_{LSD} as

$$\omega_{\text{LSD}}(r) = \frac{\Omega(r)}{C_\Omega}, \quad k_{\text{LSD}}(r) = \frac{2\pi}{C_l l} = \frac{2\pi}{\alpha_0^{1/2} C_l H(r)}, \quad (10)$$

where C_Ω and C_l are dimensionless numbers to parameterize the LSD scales, and $l = \alpha_0^{1/2} H$ is the turbulence outer scale.

A plausible ansatz for the outgoing dynamo waves is then

$$\overline{B}_{r,\phi}(t, r) \propto \sin[\omega_{\text{LSD}}(r)t - k_{\text{LSD}}(r)r], \quad (11)$$

i.e., the magnetic fields propagate at the local frequency and wavenumber. However, this approach is problematic both numerically and physically: The radial dependence of ω_{LSD} causes the magnetic fields at adjacent radial locations to gradually fall out of phase over time, and eventually give rise to spatial variations over arbitrarily small scales. In reality, LSDs cannot produce structures smaller than the turbulence scale due to turbulent diffusion. Instead, the dynamo waves are observed in simulations to be modulated into several wave packets, each having roughly constant wave frequency, with smooth boundaries mediated by turbulent diffusion. At such boundaries, the adjacent dynamo wave peaks will merge, as demonstrated in Fig. 1(b) using the data from run A01 of Zhou (2024). Therefore, a more accurate representation of disk dynamo patterns would involve the superposition of multiple wave packets, each centered at a different radius.

We assume that the disk's LSD is only active in the radial range $\xi_{\text{in}} \leq r \leq \xi_{\text{out}}$. The exact condition under which a disk LSD can efficiently operate is currently unknown, and we leave $\xi_{\text{in,out}}$ as free parameters. To construct dynamo wave packets, we assume that the i -th dynamo wave packet is centered at the radial location ξ_i , and is damped using the Gaussian profile over a distance equal to one dynamo wavelength, $2\pi/k_{\text{LSD}}(\xi_i)$. The distance between two neighboring dynamo sites, ξ_i and ξ_{i+1} , is then $2\pi/k_{\text{LSD}}(\xi_i) \propto \xi_i^{9/8}$, resulting in logarithmically distanced dynamo wave packets across the disk.

The superposition of all the dynamo waves is then

$$f_{\text{LSD}}(\Delta\varphi) = \sum_i \exp\left[-\frac{(r - \xi_i)^2}{2\Delta\xi_i^2}\right] \times \sin[\omega_{\text{LSD}}(\xi_i)t - k_{\text{LSD}}(\xi_i)r + \varphi_i + \Delta\varphi], \quad (12)$$

where we have introduced the initial phase of each wave mode, φ_i , and an overall phase, $\Delta\varphi$. To avoid the initial coherence among different wave components, we use $\varphi_i = 2\pi(i-1)/(n_{\text{dyn}} - 1)$, where n_{dyn} denotes the total number of dynamo wave components and can be calculated once k_{LSD} and $\xi_{\text{in,out}}$ are given. The particular form of φ_i is used for the sake of reproducibility, and using random initial phases does not qualitatively change our results. An overall phase difference of $\Delta\varphi = 2\pi/5$ between \overline{B}_r and \overline{B}_ϕ is empirically extracted from the simulations (Gressel 2010; Zhou 2024), so that $\overline{B}_r \propto f_{\text{LSD}}(0)$ and $\overline{B}_\phi \propto f_{\text{LSD}}(2\pi/5)$.

Finally, we assume that the variable part of the turbulent Maxwell stress response linearly to the mean fields \overline{B}_r and \overline{B}_ϕ , and hence

$$\alpha = \alpha_0 \left[1 + C_\beta f_{\text{LSD}}(0) f_{\text{LSD}} \left(\frac{2\pi}{5} \right) \right], \quad (13)$$

where C_β is roughly equal to the time average of $\overline{B}_r \overline{B}_\phi / \overline{b_r b_\phi}$, a scaling factor accounting for the relative strengths between the large- and small-scale magnetic fields. In panels (b) and (c) of Fig. 1, we compare the evolution of the normalized Maxwell stress $\overline{B}_r \overline{B}_\phi / P$ from run AO1 of Zhou (2024) to the corresponding dimensionless factor $f_{\text{LSD}}(0) f_{\text{LSD}} \left(\frac{2\pi}{5} \right)$ in Eq. (13). We adopt the disk and dynamo coefficients that are comparable to Zhou (2024): $\alpha_0 = 0.3$, $\epsilon_0 = 0.1$, $C_\Omega = 20$ and $C_l = 30$. As indicated by the arrows in the two panels, our semi-analytical model captures both the radially outgoing dynamo waves and the merging between two adjacent waves that is mediated by turbulent diffusion.

2.3. Fiducial parameters and unit conversion

Eqs. (1), (7) and (13) are the governing equations, which we implement and numerically solve in the publicly available `Pencil Code` (`Pencil Code Collaboration et al. 2021`) using sixth-order accurate finite differences and the third-order Runge-Kutta time-stepping scheme. Except for the thermal emission part, the one-dimensional diffusion equation is scale-free, and the disk dynamics is governed by the following fiducial dimensionless parameters,

$$r_{\text{out}}/r_0 = 500, \quad \epsilon_0 = 0.05, \quad \alpha_0 = 0.05. \quad (14)$$

The fiducial dimensionless dynamo parameters are

$$C_\Omega = 30, \quad C_l = 20, \quad \xi_{\text{in}}/r_0 = 1, \quad \xi_{\text{out}}/r_0 = 100, \quad (15)$$

and we use $C_\beta = 0.05$ and $C_\beta = 0.3$ for the fiducial runs W and S for the weak and strong variability cases, respectively.

We use the initial condition $\Sigma(t=0, r) = \Sigma_0 = 10^{-5}$ in code units, and the same value is used as the density floor to avoid negative values of the surface density. At both the inner and the outer radial boundaries, Σ is kept fixed, with $\Sigma(r_0) = \Sigma_0$ as a sink and $\Sigma(r=r_{\text{out}}) = 10^3 \Sigma_0$ as a mass source.

To convert code units to physical units, we adopt the fiducial length scale and black hole mass

$$r_0 = 2r_g = \frac{2GM_{\text{BH}}}{c^2}, \quad M_{\text{BH}} = 10^8 M_\odot. \quad (16)$$

The accretion rate at the outer boundary [calculated using Eq. (2)] is used to scale Σ to physical units by setting the mean Eddington ratio $\eta_{\text{Edd}} = L/L_{\text{Edd}}$ in the steady state to the fiducial value 0.2, which also fixes the temperature unit conversion. To convert to the observed flux, we adopt the distance $d = 100$ Mpc.

3. Results

In this section, we first show the results from the two fiducial runs which only differ in their values of C_β . We demonstrate some of the persistent features of our model, namely the linear rms-flux relation, DRW-like PSDs and the scaling relations of τ_d with photon wavelengths and SMBH masses, and discuss their physical origins along the way. We then investigate how τ_d depends on the other disk and dynamo parameters, including C_Ω , ξ_{in} , ξ_{out} and α . We also make a comparison with the L97 model at the end of this section.

3.1. The linear rms-flux relation

In Fig. 2, we present the light curves of runs W and S in their steady states calculated from Eq. (5), and examine their rms-flux relations. For each run, the light curve is divided into 600 intervals, and the mean and the standard deviation of each interval are depicted as the blue dots in the right panels. Due to the significant scatter observed in the latter, the data is further binned into 20 groups, with the average value of each group represented by the red dots and the error bars representing the 1σ deviation. These red dots clearly follow a linear rms-flux relation. The histograms of the logarithm of the mean normalized luminosities, shown in the insets of panels (b) and (d), reasonably approximate Gaussian distributions.

The linear rms-flux relation and the log-normal distribution of the flux together reflect the nonlinearity of the random process characterizing the light curves (Uttley & McHardy 2001; Uttley et al. 2005). Such nonlinearity has also been seen in the work of Turner & Reynolds (2021), where α is assumed to be driven by a stochastic forcing. The similar results obtained using our physics-based model and their phenomenological model suggest that the nonlinearity does not originate from the physical processes driving the fluctuations, but is due to the propagation of these fluctuations coupled to the accretion dynamics.

3.2. DRW-like PSDs of accretion rates

In this work, we focus on the thermal emission from optically thick disks. However, the variability of the accretion rate, which directly reflects the release of gravitational energy, is a fundamental aspect that applies regardless of the disk's emission mechanisms. By investigating the accretion variability, we can gain insights that may also be applicable to studies involving optically thin disks, where the emission mechanisms differ but the underlying energy source remains the same.

In Fig. 3, we present the time series and the corresponding PSDs of \dot{M} at four selected radii, as calculated using Eq. (2). For run S, \dot{M} occasionally shows large negative values, indicating outward mass transfer and reflecting the significant variations in the viscosity parameter. For both runs W and S, the PSDs are flat at low frequencies and follow an approximate $\propto f^{-2}$ power law at high frequencies, consistent with the DRW model. The break frequency f_{break} which demarks the transition from a white-noise spectrum to the f^{-2} one can be approximately identified as the peak in each PSD, and is plotted against r in the insets of panels (b) and (d). We see that f_{break} closely follows $\propto r^{-3/2}$, and hence the damping time scale $\tau_d = (2\pi f_{\text{break}})^{-1} \propto r^{3/2}$, implying a strong correlation between the damping time scale with the local variability time scale $C_\Omega \Omega^{-1}$.

The DRW-like PSDs of \dot{M} , or equivalently the energy release rate, can potentially be connected to observations in other wavelength bands, such as X-ray (Zhang et al. 2024) and sub-millimeter bands (Chen et al. 2023). These wavelengths typically trace the innermost regions of the accretion disks and may also be linked to jet activity. Additionally, when reprocessing is considered (Sun et al. 2020; Hagen et al. 2024), X-ray emission serves as a key driver of variability, with the disk being illuminated by flares originating from the corona. Our model naturally produces DRW-consistent noise, which can provide a complementary component for the variability source in such models.

In the rest of this subsection, we provide a qualitative explanation of the flattening of the PSDs at low frequencies by modeling the inward propagation of mass flux fluctuations. We first justify the multiplicative nature of these fluctuations, which

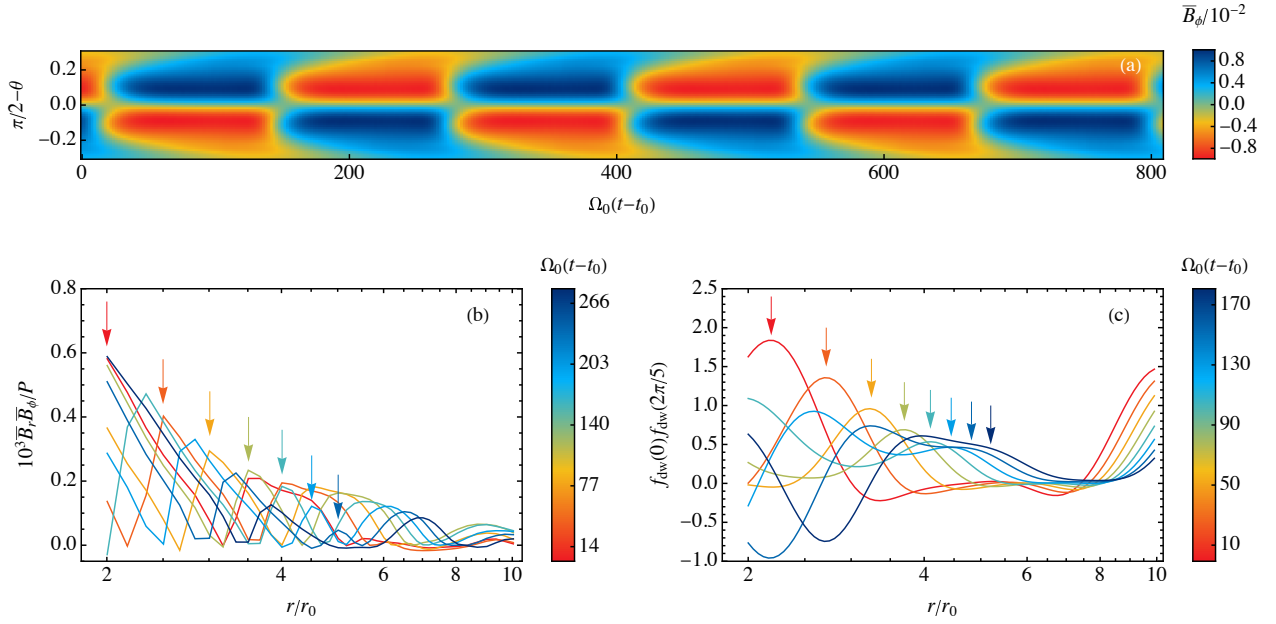


Fig. 1. Comparing our prescription Eq. (13) with the global disk dynamo simulation in Zhou (2024). Panels (a) and (b) are outputs of run A01 in Zhou (2024). Panel (a) shows the space-time diagram of $\bar{B}_\phi(t, \theta)$ at $r = 2r_g$, starting from $t_0 = 10^4 \Omega_0^{-1}$, and θ is the latitude. Panel (b) plots the normalized Maxwell stress at $\theta = 0.15$, with $t_0 = 5960 \Omega_0^{-1}$. Panel (c) shows the varying part in Eq. (13) using the parameters $\alpha = 0.3$, $\epsilon_0 = 0.1$, $C_l = 30$, and $C_\Omega = 20$, starting from $t_0 = 2 \times 10^6 \Omega_0^{-1}$. The arrows in panels (b) and (c) remark a particular peak in each panel which propagates, damps, and merges with a later peak.

manifests itself in the linear rms-flux relation and the log-normal distribution of the flux (Uttley & McHardy 2001; Uttley et al. 2005). Consider the disk to be composed of thin concentric rings (labeled by $i = 1, 2, \dots$) with width $d_i \ll r_i$ and initially in a steady state with uniform accretion rate \dot{m} . In the i -th ring, the surface density Σ_i and viscosity ν_i are approximately uniform, and $\dot{m} = 3\pi\nu_i\Sigma_i$ for any i . Suppose during a time interval Δt , the viscosity ν_i is increased to $(1 + f_i)\nu_i$ in the i -th ring. The accretion rate correspondingly increases to $\dot{m}_i \approx 3\pi(1 + f_i)\nu_i\Sigma_i \approx (1 + f_i)\dot{m}$. The increase in the surface density of its inner neighbor, the $(i - 1)$ -th ring, will be

$$\Delta\Sigma_{i-1} = \frac{(\dot{m}_i - \dot{m})\Delta t}{2\pi r_{i-1} d_{i-1}} = \frac{f_i \Delta t}{2\pi r_{i-1} d_{i-1}} \dot{m}. \quad (17)$$

Similarly, consider an independent change of the viscosity on the $(i - 1)$ -th ring, from ν_{i-1} to $(1 + f_{i-1})\nu_{i-1}$. From the $(i - 1)$ -th to the $(i - 2)$ -th ring, the accretion rate will be

$$\begin{aligned} \dot{m}_{i-1} &\approx 3\pi(1 + f_{i-1})\nu_{i-1}(\Sigma_{i-1} + \Delta\Sigma_{i-1}) \\ &= (1 + f_{i-1}) \left(1 + \frac{3\nu_{i-1}\Delta t}{2r_{i-1}d_{i-1}} f_i \right) \dot{m}. \end{aligned} \quad (18)$$

Δt can be estimated as the time needed for accretion to become uniform over the $(i - 1)$ -th ring, i.e., $\Delta t = d_{i-1}/(3\nu_{i-1}/2r_{i-1})$, so that the prefactor of f_i in Eq. (18) is just unity. Iterating the derivation, we find that the variability of the accretion rate in the inner disk region is approximately multiplicative,

$$\dot{m}_j \approx \dot{m} \prod_{k=j}^i (1 + f_k), \quad 1 \leq j \leq i. \quad (19)$$

If the fluctuation on each ring can be regarded as independent (e.g., by setting d_i equal to one dynamo wavelength), then the PSD of \dot{m}_j is the convolution of the PSDs of each individual f_k in Eq. (19) (Ingram & van der Klis 2013). Assuming that each

of these uncorrelated fluctuations has a broken power-law PSD with a non-negative slope at low frequencies (i.e., not dominated by long-time variabilities), the successive convolutions of such PSDs leads to a broken power-law PSD with a flat low-frequency part (see Appx. A for a proof). Therefore, the multiplicative nature of the accretion rate variability explains its flat PSD at low frequencies.

3.3. Specific fluxes and damping times

We now continue our analysis of the results from the fiducial runs, and examine the specific fluxes F_λ calculated using Eq. (4). As mentioned before, we use $M_{\text{BH}} = 10^8 M_\odot$ and $\eta_{\text{Edd}} = 0.2$ as the fiducial values for converting code units to physical units.

We fit for the damping time using the covariance function

$$\text{cov}(F_\lambda)(\Delta t) = \left\langle [F_\lambda(t + \Delta t) - \langle F_\lambda \rangle] [F_\lambda(t) - \langle F_\lambda \rangle] \right\rangle, \quad (20)$$

where $\langle \cdot \rangle$ indicates a time average over t .¹ The damping time scale $\tau_d(\lambda)$ is found by fitting $\text{cov}(F_\lambda)(\Delta t)$ at small Δt using the linear form, $\propto 1 - \Delta t/\tau_d$. We then calculate and bin the PSDs for each λ and fit for its power-law part. The starting frequency of the power-law region is fixed to be $f_1 = 10^{0.5} (2\pi\tau_d)^{-1}$. To determine at which frequency the power law ends, we first estimate the noise level by taking the mean value of the last four points in the binned PSD, and then find the lowest frequency f_2 at which the PSD amplitude is less than 1.1 times the noise level. A power law is then fitted to the data in the frequency range between f_1 and f_2 . Finally, the frequency f_3 at which the fitted power law relation intersects with the noise level is calculated and the noise time scale is defined as $\tau_{\text{noise}} = (2\pi f_3)^{-1}$.

¹ For discrete time series $g(t)$ with step size dt , we use $\text{cov}(g)(idt) = N^{-1} \sum_{j=1}^{N-i} (g_i - \bar{g})(g_{i+j} - \bar{g})$ where N is the length of the data and $\bar{g} = N^{-1} \sum_{i=1}^N g_i$. The factor of N^{-1} rather than $(N - i)^{-1}$ in the definition of $\text{cov}(g)$ ensures that the estimate is unbiased.

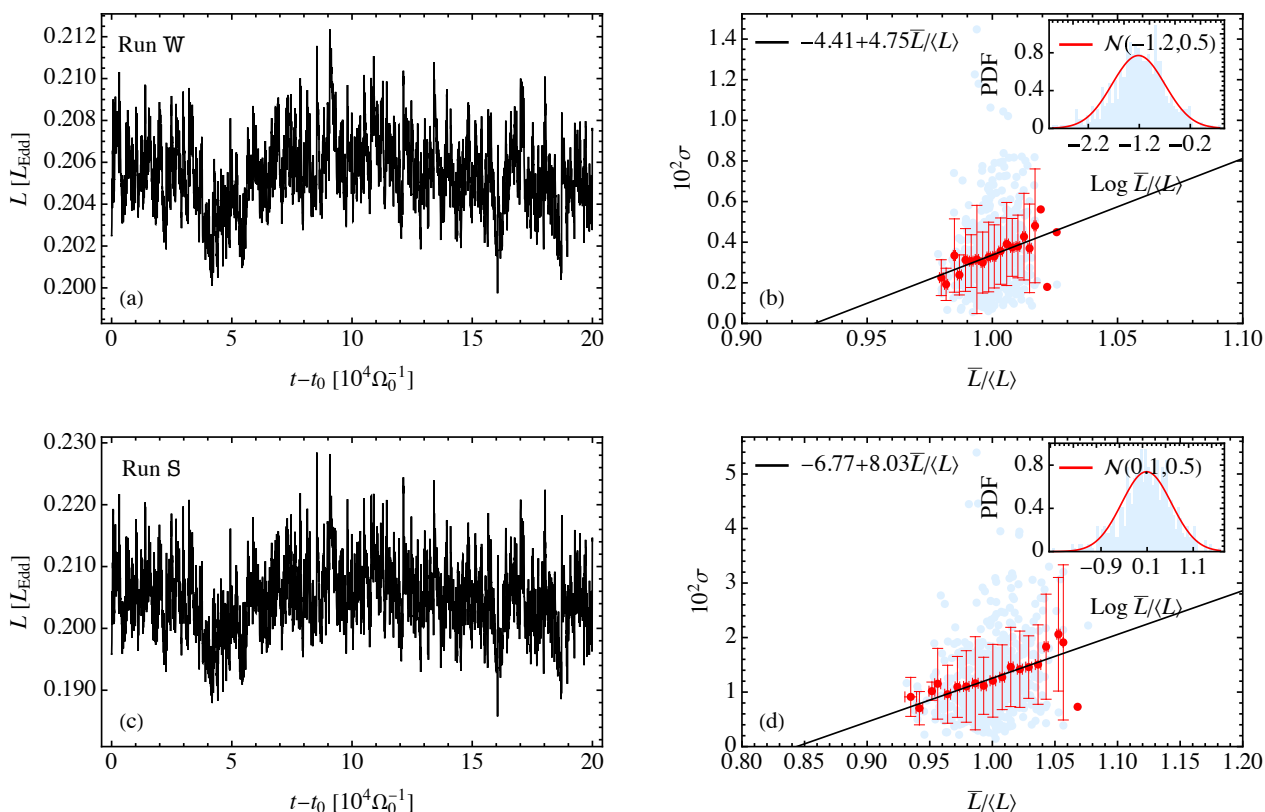


Fig. 2. Results for the fiducial run W with $C_\beta = 0.05$ (top) and run S with $C_\beta = 0.3$ (bottom): Light curves normalized by the Eddington luminosity L_{Edd} (left), and the rms-flux relations (right). The insets in the right panels show the histograms of the normalized luminosity on a log-linear scale and its fitted log-normal distribution.

For the two fiducial runs, the PSDs for the representative value $\lambda = 2500\text{\AA}$, their binned values, the fitted power laws, and the damping and the noise frequencies are shown in Fig. 4. For both, the PSDs resemble DRW-like shapes at low to intermediate frequencies, and flatten out at high frequencies (Mushotzky et al. 2011; Zu et al. 2013). It is worth noting that the input variability in Eq. (13) is not prescribed to follow a DRW process; rather, the PSD of α at a fixed radius approximately exhibits a single peak corresponding to the local dynamo frequency. Interestingly, the overall disk dynamics naturally evolve to produce a DRW-like PSD. As we will discuss in Sec. 3.5, implementing the L97 model using Poisson processes does not reproduce the DRW-shaped PSD, although the stronger high-frequency variability persists. A more detailed comparison between the L97 model and ours is deferred to that subsection.

To examine the λ dependence of the time scales, the same fitting procedure is done for a wider range of wavelengths. For each run, we use the maximum of the time-averaged temperature \bar{T}_{max} to define a wavelength normalization,

$$\lambda_0 = \frac{hc}{k_B \bar{T}_{\text{max}}}. \quad (21)$$

Since $T^4 \propto \nu \Sigma \Omega^2 \propto M_{\text{BH}} \dot{M} \propto M_{\text{BH}}^2 \eta_{\text{Edd}}$, we have $\lambda_0 \propto M_{\text{BH}}^{-1/2} \eta_{\text{Edd}}^{-1/4}$. In Fig. 5, we present the dependence of the damping and noise time scales on λ . The damping time scale (solid dots) exhibits a transition from $\tau_d \propto \lambda^2$ to a plateau, and the critical wavelength for the flattening to happen is empirically found to be

$$\lambda_{\text{flat}} \simeq 4\lambda_0 \simeq 3000\text{\AA} \left(\frac{M_{\text{BH}}}{10^8 M_\odot} \right)^{-1/2} \left(\frac{\eta_{\text{Edd}}}{0.2} \right)^{-1/4}. \quad (22)$$

The λ^2 dependence is expected if photons at wavelength λ predominantly originate from the ring around r_λ where the thermal spectrum peaks at λ (see MacLeod et al. 2010, and also Sec. 4). However, at moderately large wavelengths, the λ dependence flattens out, as the emission from lower-energy photons arises not only from the ring at r_λ but also from regions at $r < r_\lambda$, leading to a blending of their respective time scales. This flattened part is consistent with the weak scaling $\propto \lambda^{0.17}$ from MacLeod et al. (2010). To justify that the weak dependence on λ is due to time scale mixing, we artificially exclude the flux contribution from $r < r_\lambda$ and re-calculate τ_d . This yields the empty circles in Fig. 5, and the fitted τ_d remains $\propto \lambda^2$ for all the wavelengths considered.

In the same figure we also find that the noise time (squares) can be empirically fitted as $\tau_{\text{noise}} \propto \lambda$. The slower increasing in the time scale than the Keplerian profile $\propto r_\lambda^{3/2} \propto \lambda^2$ can again be attributed to that the contribution from $r < r_\lambda$ becomes non-negligible, and hence the noise time scale for a given λ is determined by the dynamics at $r < r_\lambda$.

To compare the values of τ_{noise} from our model with observations, we convert τ_{noise} at 5000\AA into physical units using the parameters of the four *Kepler* AGNs: Zw 229-15, KA 1925+50, KA 1858+48, and KA 1904+37, whose PSDs were analyzed in Mushotzky et al. (2011). With the high-cadence data from *Kepler*, these AGNs have some of the most accurately determined noise time scales, making them ideal for comparison. The black hole masses, Eddington ratios, and the fitted τ_{noise} values are listed in Table 1. For these four sources, our model predicts τ_{noise} values ranging from ~ 1.5 to 5 days, corresponding to frequencies between 3.7×10^{-7} and 1.3×10^{-6} Hz. These time scales are noticeably longer than those shown in Fig. 3 of Mushotzky et al.

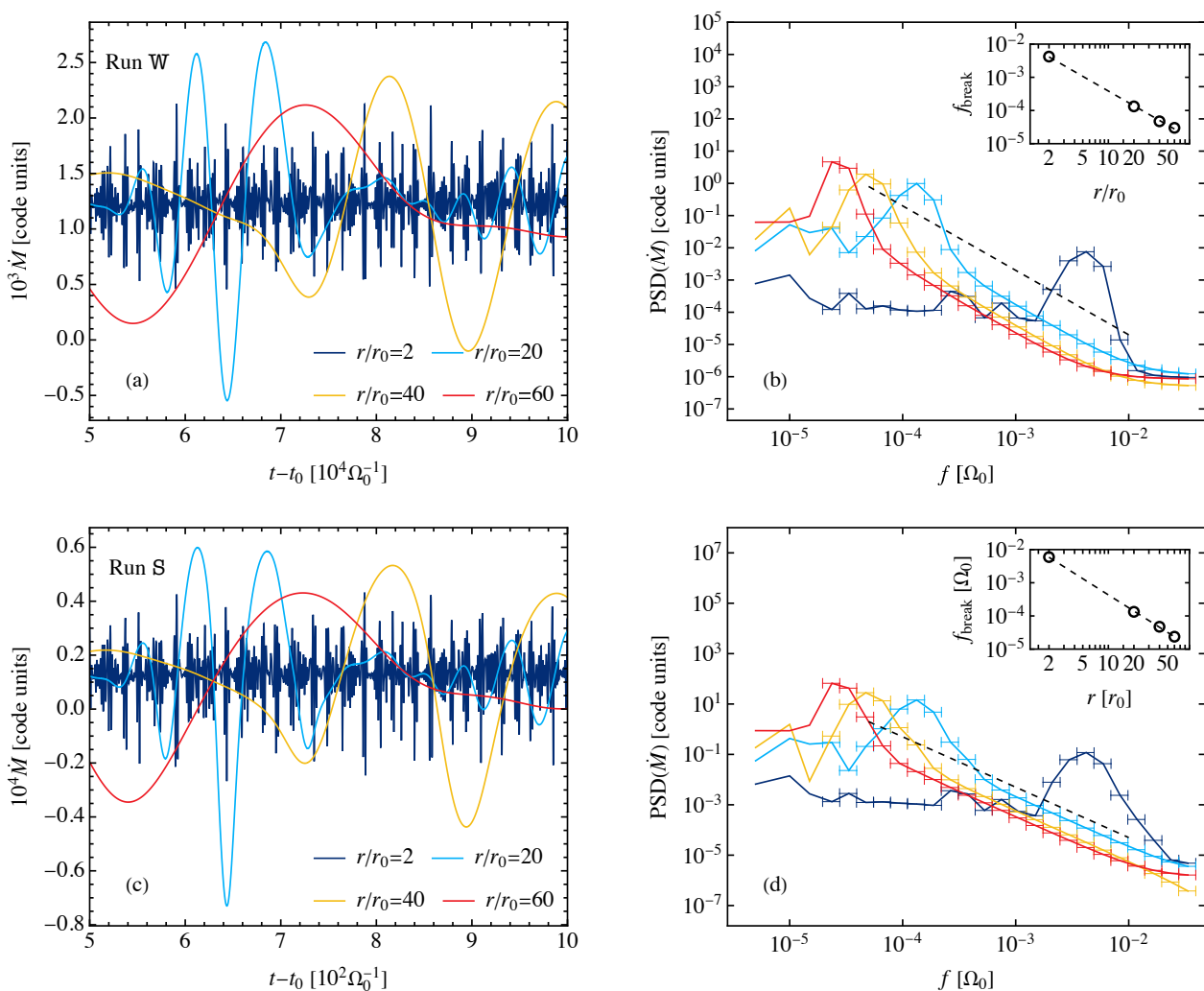


Fig. 3. Results for the fiducial run W with $C_\beta = 0.05$ (top) and run S with $C_\beta = 0.3$ (bottom): The time series of accretion rate during a short time interval at four selected radii (left), and the PSDs calculated from the full time interval and binned with a width of 0.15 dex (right). The dashed lines indicate $\propto f^{-2}$. The insets plot the breaking frequency f_{break} as a function of the radius, and a power-law fitting gives $f_b \propto r^{-1.47 \pm 0.03}$ and $f_b \propto r^{-1.62 \pm 0.02}$ for panels (b) and (d), respectively.

(2011), suggesting that under the parameters chosen, our model produces too much variability at shorter time scales. Modifying the dynamo parameters may change the values of τ_{noise} to match the observation values better. In Sec. 3.4, we demonstrate that C_β is such a parameter with which τ_d scales weakly but τ_{noise} scales strongly (as is already evident from Fig. 5). Hence by adjusting C_β it is possible to match both τ_d and τ_{noise} with observations.

Finally, using the data from runs W and S, we compute τ_d at 2500\AA for $M_{\text{BH}} \in [10^4, 10^{10}]M_\odot$ and $\eta_{\text{Edd}} \in [0.02, 0.4]$ to examine its dependence on M_{BH} . The results are shown in Fig. 6, and the difference of the calculated τ_d is minor between the two runs. The $\tau_d - M_{\text{BH}}$ scaling law varies when η_{Edd} is changed: At $M_{\text{BH}} \lesssim 10^6 M_\odot$, the scaling $\tau_d \propto M_{\text{BH}}$ is roughly independent of η_{Edd} , while at larger M_{BH} , the dependence on η_{Edd} is stronger, introducing a weaker scaling between τ_d and M_{BH} when η_{Edd} is small. At the latter $M_{\text{BH}} \gtrsim 10^6 M_\odot$ mass range, the scaling $\tau_d \sim M_{\text{BH}}^{0.5}$ is in agreement with that of the radiation flux-averaged orbital time at a given wavelength (Wolf et al. 2024). In Fig. 6, over-plotted is the data from Fig. 1 of Burke et al. (2021), who showed that $\tau_d \propto M_{\text{BH}}^{0.38}$. In the range $M_{\text{BH}} \gtrsim 10^6 M_\odot$, our variability model reasonably well covers the data, whereas at lower M_{BH} the scaling deviates. We provide a possible expla-

nation relating to the dependence of dynamo properties on M_{BH} and \dot{M} in Sec. 4.

3.4. Varying parameters

Based on run W with $M_{\text{BH}} = 10^8 M_\odot$ and $\eta_{\text{Edd}} = 0.2$, we systematically vary one dynamo or disk parameter at a time to investigate how τ_d and τ_{noise} scale with each. The results, shown in Fig. 7, indicate that the most significant dependencies of τ_d are with C_Ω (with a slope of ≈ 1.6) and ξ_{out} (with a slope of ≈ 0.5). The former reflects the direct relationship between the dynamo time scale and accretion variability, while the latter arises from the more extended emission region when ξ_{out} is increased. These findings suggest that although the cycle periods of the LSDs and the size of their active regions are not directly observable, they nevertheless play critical roles in the variability of disk emissions. Future work could focus on leveraging these results to infer the dynamo properties from AGN light curves.

3.5. Comparison with Lyubarskii (1997)

To conclude this section, we compare our model with the work by Lyubarskii (1997). The primary distinction between the L97

Table 1. Parameters and the fitted values of τ_{noise} for the four *Kepler* AGN sources in [Mushotzky et al. \(2011\)](#). The references for the disk parameters are listed in the last column. Except for M_{BH} and η_{Edd} , the simulation parameters are the same as run W.

Source name	KIC #	$\log_{10} M_{\text{BH}}/M_{\odot}$	η_{Edd}	τ_{noise} [days]	Reference
Zw 229-15	6932990	6.91	0.125	1.48	Smith et al. (2018)
KA 1925 + 50	12158940	8.04	0.013	5.32	Smith et al. (2018)
KA 1858 + 48	11178007	6.91	0.2	1.54	Pei et al. (2014)
KA 1904 + 37	2694186	7.66	0.089	4.89	Smith et al. (2018)

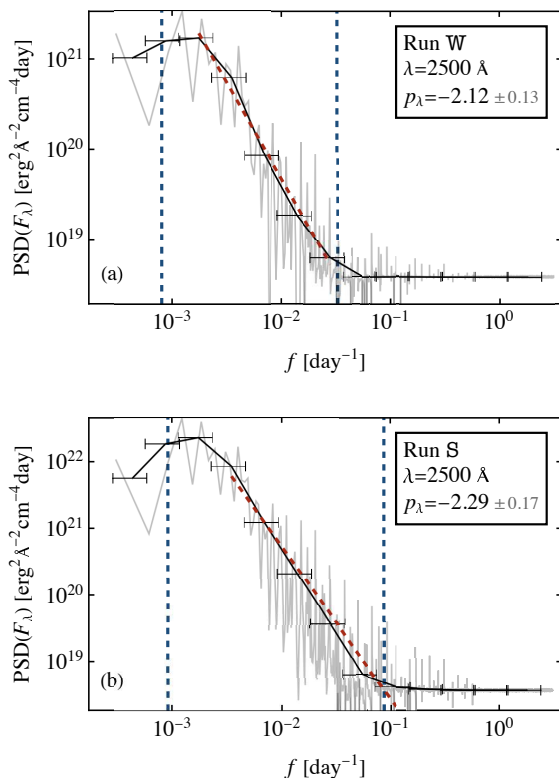


Fig. 4. PSDs of the radiation fluxes at $\lambda = 2500\text{\AA}$ for the fiducial runs W (a) and S (b). For each panel, the original and the binned spectra are shown in gray and black, respectively; the red dashed lines are the fits of the power-law parts; the frequencies corresponding to the damping time scale ($1/2\pi\tau_{\text{d}}$) and the noise time scale ($1/2\pi\tau_{\text{noise}}$) are marked by the left and right vertical dashed lines, respectively.

model and ours lies in the treatment of fluctuations: L97 assumes they are spatially uncorrelated, whereas we consider them to be correlated within a dynamo wavelength. Specifically, in the L97 model, a stochastic component $\vartheta(t, r)$ is introduced into the viscosity parameter,

$$\alpha = \alpha_0[1 + \vartheta(t, r)], \quad (23)$$

where ϑ is a random variable with rms value ϑ_{rms} , uncorrelated in r but correlated in t with a correlation time $\tau_{\vartheta}(r)^2$.

The L97 model assumes that the value of τ_{ϑ} is comparable to the viscous time $r^2/\nu = \alpha_0^{-1}\epsilon_0^{-2}\Omega_0^{-1}\tilde{r}^{5/4}$. In our analysis, we parameterize it as $\tau_{\vartheta}(r) = C_{\text{L97}}\Omega_0^{-1}\tilde{r}^{p_{\text{L97}}}$, allowing it to be shorter than the viscous time. Furthermore, at each radius,

² In our simulations, the temporal correlation is implemented by generating a random number $\text{rand} \in [0, 1)$ at each grid and each time step, and comparing it with $\text{dt}/\tau_{\vartheta}$, where dt is the current time step. If the former is smaller, then the value of ϑ at location r is updated. In the case where dt is a constant, ϑ at a given r follows the Poisson process.

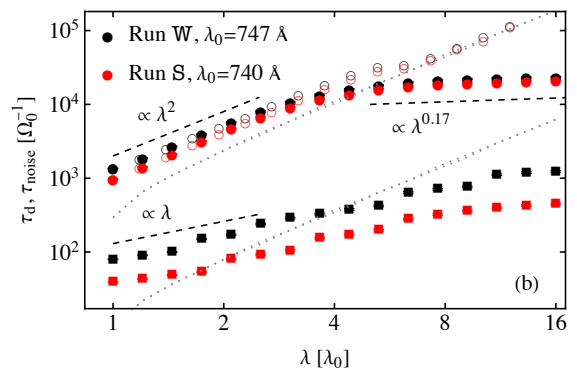


Fig. 5. Damping (circles) and noise (squares) time scales for the fiducial runs W (black) and S (red), with $M_{\text{BH}} = 10^8 M_{\odot}$ and $\eta_{\text{Edd}} = 0.2$. The empty circles denote the damping time scales when the emission only includes the disk region at $r \geq r_{\lambda}$. The dashed lines are scaling laws to guide the eye, and the dotted curves are the orbital time scale $2\pi/\Omega(r_{\lambda})$ (lower) and the dynamo time scale $2\pi C_{\Omega}/\Omega(r_{\lambda})$ (upper), respectively. The errors bars for the black and red data points are too small to be seen.

ϑ is drawn from a uniform probability distribution in the range $[-0.02, 0.02]$, yielding $\vartheta_{\text{rms}} \approx 0.012$.

We consider two cases: (i) run L97V, where $C_{\text{L97}} = \alpha_0^{-1}\epsilon_0^{-2}$ and $p_{\text{L97}} = 5/4$ corresponding to the original proposal of [Lyubarskii \(1997\)](#) using the viscous time scale, and (ii) run L97D, where $C_{\text{L97}} = 30$ and $p_{\text{L97}} = 3/2$, which yields a variability timescale roughly comparable to that of our fiducial dynamo models. The time series of the accretion rate at representative radii, their PSDs, $P_{\dot{M}}$, and the PSD of F_{λ} at 2500\AA from the two runs are shown in Fig. 8. According to [Lyubarskii \(1997\)](#), $P_{\dot{M}}(f)$ scales as f^{-1} at frequencies lower than $1/\tau_{\vartheta}$, which frequencies are indicated by the vertical dashed lines in the middle column. To guide the eye, a black dashed line indicating $\propto f^{-1}$ is also plotted. In the right column, the fitted frequencies corresponding to the damping and the noise time scales are marked by the vertical dashed blue lines, while $1/\tau_{\vartheta}$ is shown in black. We see that the L97 model generally does not produce PSDs that exhibit clear low-frequency plateaus. For the L97D run, the fitted damping times appear too large, where $\tau_{\text{d}} \approx 6000$ days if $M_{\text{BH}} = 10^8 M_{\odot}$ and $\eta_{\text{Edd}} = 0.2$. This suggests that simply assigning the correct variability time scale at each radius is insufficient to reproduce the DRW-shaped PSD with the correct damping time. Two additional factors may be crucial: (i) the nature of the PSD at each radius, where the L97 model assumes a white noise spectrum while our dynamo model exhibits a peaked spectrum, and (ii) the spatial correlation of fluctuations, with the L97 model assuming no spatial correlation and our model incorporating a correlation length scale of $2\pi/k_{\text{LSD}}$.

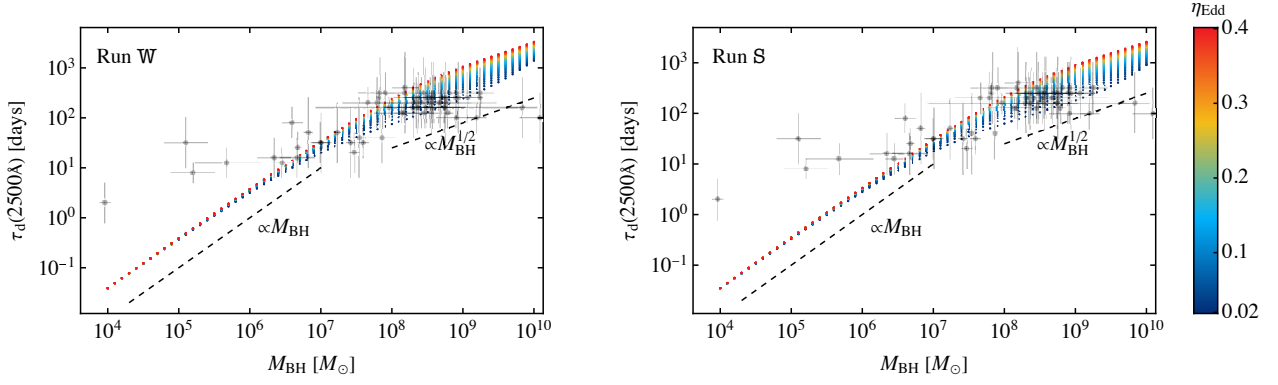


Fig. 6. Damping time τ_d at 2500\AA versus M_{BH} from runs W (left) and S (right). The data points are color-coded based on their respective η_{Edd} values. The gray points with error bars represent observational data from Fig. 1 of [Burke et al. \(2021\)](#) for reference.

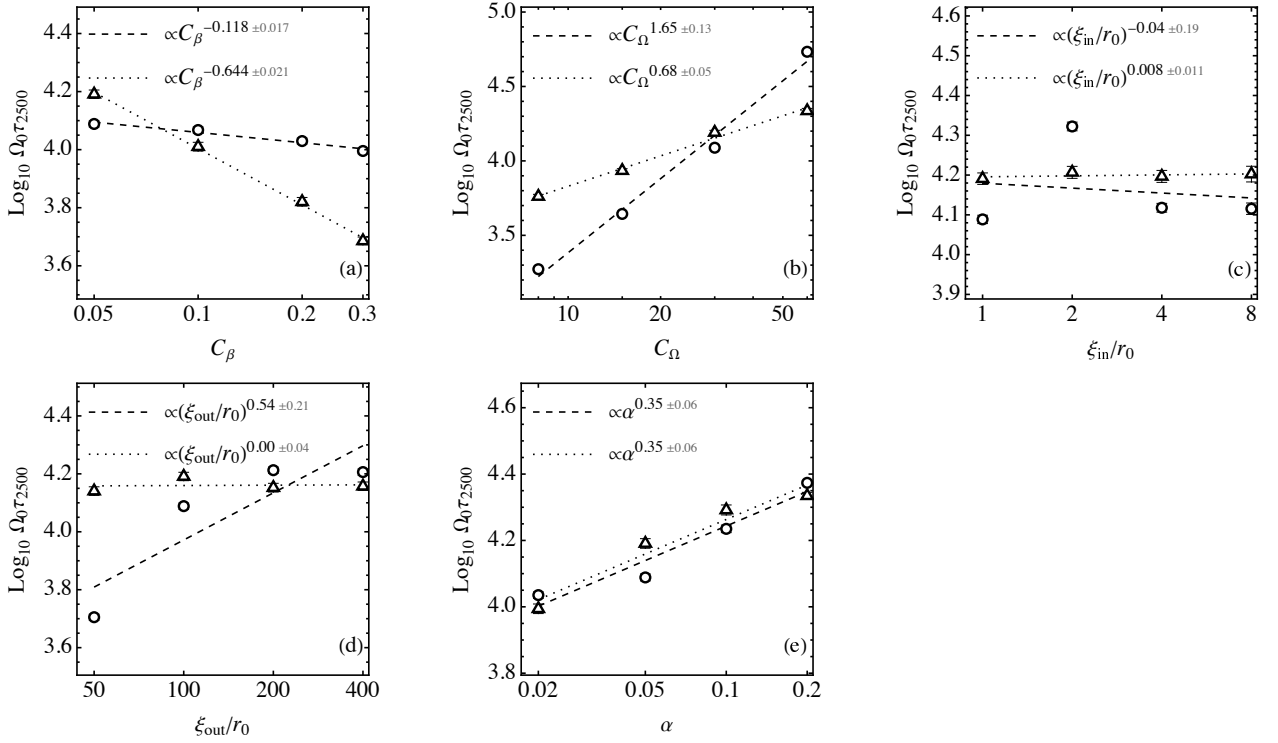


Fig. 7. Dependence of the damping time scale τ_d (circles) and the noise time scale τ_{noise} (triangles) at 2500\AA on the dynamo and disk parameters in our model W run.

4. Discussion & Conclusion

Studies of AGN light curves have uncovered intriguing properties in their UV/optical variabilities, particularly the scaling laws between the damping time τ_d and AGN parameters. Notably, τ_d shows only a weak dependence on the rest-frame luminosity ([MacLeod et al. 2010](#)), suggesting that this scaling is a universal feature of accretion disks surrounding SMBHs. In this work, we propose a possible mechanism—quasi-periodic large-scale disk dynamos—that can explain many of the observed feature of the AGN variabilities, including the linear rms-flux relation and the log-normal distribution of the light curve, and the DRW-like PSD for the disk thermal spectrum. For a given AGN, τ_d exhibits a varying scaling index with the photon wavelength λ , transiting from 2 for short wavelengths to $\lesssim 0.2$ for longer wavelengths. Furthermore, we show that for $M_{\text{BH}} \gtrsim 10^6 M_{\odot}$, the $\tau_d - M_{\text{BH}}$ scaling aligns with observations when accounting for the uncertainties in the Eddington ratio η_{Edd} . However, explain-

ing the scaling below $10^6 M_{\odot}$ may require further refinement of the dynamo models, as discussed below.

Consider two limiting cases regarding the emission site of photons at wavelength λ . In the first case, we assume that they come from a narrow ring at radius r_{λ} whose thermal emission peaks at λ (see also [MacLeod et al. 2010](#)). The surface temperature of the ring is $T \propto \lambda^{-1}$, and we have

$$\lambda \propto T^{-1} \propto D^{-1/4} \propto M_{\text{BH}}^{-1/4} \dot{M}^{-1/4} r_{\lambda}^{3/4}. \quad (24)$$

Hence

$$\tau_d(M_{\text{BH}}, \lambda) \propto M_{\text{BH}}^{-1/2} r_{\lambda}^{3/2} \propto \dot{M}^{1/2} \lambda^2 \propto \eta^{-1/2} \eta_{\text{Edd}}^{1/2} M_{\text{BH}}^{1/2} \lambda^2, \quad (25)$$

where $\eta = L/\dot{M}c^2$. In the other limit, photons at any wavelength have equal contributions from the whole disk, and thus τ_d loses its dependence on λ . The only relevant time scale in the problem is then r_g/c , giving

$$\tau_d(M_{\text{BH}}, \lambda) \propto r_g/c \propto M_{\text{BH}} \lambda^0. \quad (26)$$

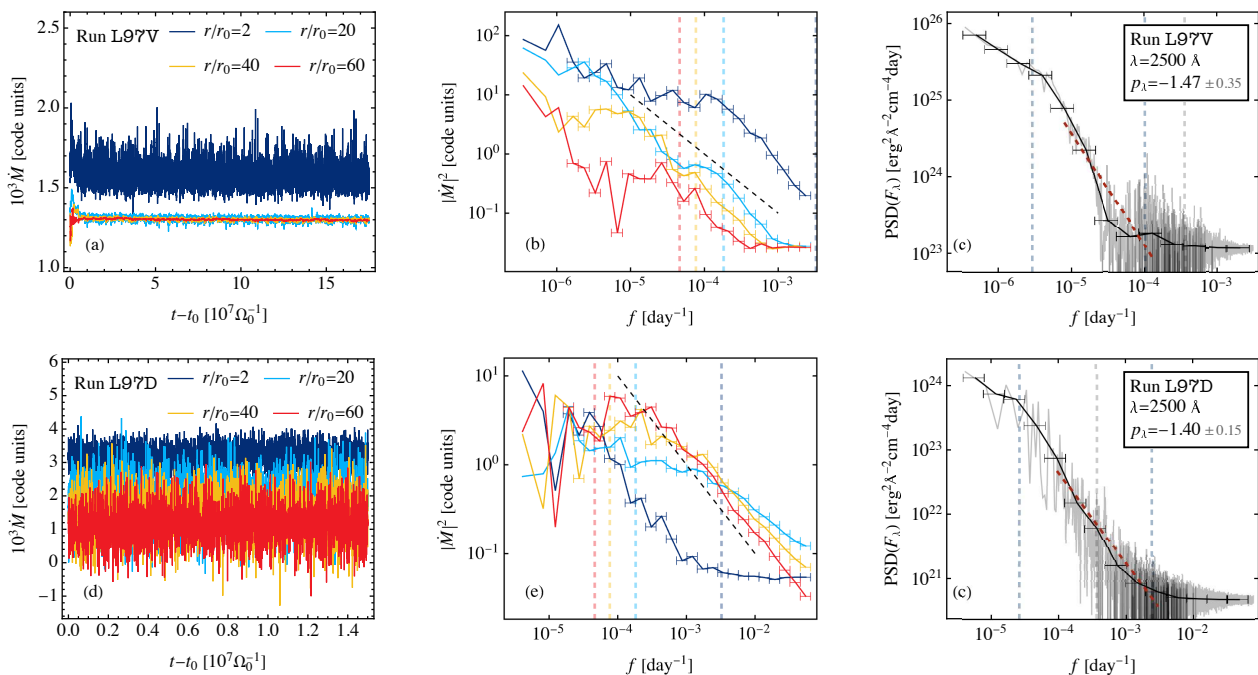


Fig. 8. Results for runs L97V (top) and L97D (bottom). The three columns plot the time series of accretion rates at representative radii (left), their PSDs (middle, with the $1/\tau_\theta$ frequencies marked by the vertical dashed lines), and the PSD of F_λ at 2500Å (right). The vertical dashed lines in the right column indicate the damping (left), $1/\tau_\theta$ (middle), and noise (right) frequencies,

In reality, we expect an intermediate scenario where photons at wavelength λ originate from a finite region around r_λ . Thus, we would expect a scaling exponent for the $\tau_d - M_{\text{BH}}$ relation between $1/2$ and 1 , and for $\tau_d - \lambda$ between 2 and 0 . Observationally, a value for the index of M_{BH} of less than $1/2$ is commonly supported (MacLeod et al. 2010; Burke et al. 2021), which suggests that factors beyond a simplistic emission site geometry, such as magnetic fields, could influence the observed variability.

The large-scale magnetic fields in accretion disks can originate either from *in situ* dynamo processes or through the advection of magnetic field lines from the surrounding environment. For the former, Fig. 7 illustrates how the damping time scale is closely tied to the large-scale dynamo properties. However, the precise dependence of dynamo parameters, such as cycle periods and coherence lengths, on both M_{BH} and \dot{M} remains unclear and requires further exploration. The different damping time scales in the low and high states of AGNs (Ren et al. 2024) may also be explained by the different operating dynamos in thin and thick disks. Regarding advected fields, a greater advection efficiency would seemingly reduce the accretion variability by adding a non-fluctuating component to the disk field. The efficiency of advection is influenced by several factors, including the coronal magnetic fields, the vertical structure of the disk, and disk winds (Beckwith et al. 2009; Guilet & Ogilvie 2012, 2013; Cao & Spruit 2013). Accounting for (i) how the dynamo processes are influenced by accretion physics, and (ii) the role of advected fields, could help improve the agreement between the current variability model and the observational data.

Acknowledgment

We thank Ying Zu, Eric Blackman and Mouyuan Sun for insightful discussions. HZ acknowledges support from the National Natural Science Foundation of China (No. 12403020), and the

China Postdoctoral Science Foundation (No. 2023M732251). The numerical simulations in this work were carried out on the Astro cluster supported by Tsung-Dao Lee Institute.

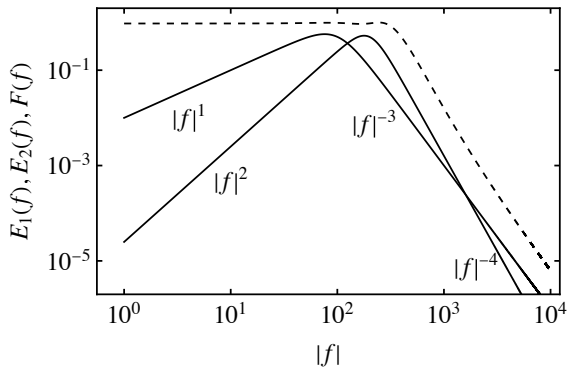


Fig. A.1. $F(f)$ (dashed) is the convolution of two broken power-laws E_1 and E_2 (solid), displaying a flat low-frequency end and a $\propto |f|^{-3}$ high-frequency end.

Appendix A: Convolution of two broken power laws

The Fourier transform $\tilde{s}(f)$ of a real-valued time series $s(t)$ has the property $\tilde{s}(f) = \tilde{s}^*(-f)$, where the asterisk denotes the complex conjugate. We assume that the PSD of $s(t)$ is a broken power law with a positive slope α_1 at low-frequencies and a negative slope α_2 at high-frequencies, and define the square of the Fourier amplitudes of \tilde{s} as

$$E(f; f_p, \alpha_1, \alpha_2) \equiv |\tilde{s}(f)|^2, \quad -\infty < f < \infty, \quad (\text{A.1})$$

so that $E(f)$ has a slope $\alpha_1 > 0$ when $|f| < f_p$, and a slope $\alpha_2 < 0$ when $|f| > f_p$. The PSD of $s(t)$ is $2E(|f|)$.

By definition, the convolution of two such functions $E_1(f) = E(f; f_1, \alpha_1, \alpha_2)$ and $E_2(f) = E(f; f_2, \alpha_3, \alpha_4)$ is

$$F(f) = \int_{-\infty}^{\infty} E_1(f')E_2(f-f') df'. \quad (\text{A.2})$$

Note that $E_1(f)$ and $E_2(f)$ only have compact support near $|f| = f_1$ and $|f| = f_2$, respectively, and hence the main contributors to the integral (A.2) is from two regions: (i) $|f'| \simeq f_1$, and (ii) $|f-f'| \simeq f_2$.

We now consider the limiting behaviors of $F(f)$. When $|f| \ll f_{1,2}$, the E_2 term in the integrand can be expanded using $|f| \ll |f'|$ since compact support only occurs at $|f'| = f_{1,2}$. The leading order is just $E_2(f')$ and independent of f , yielding $F(f) \propto |f|^0$.

When $|f| \gg f_{1,2}$, we consider the contributions from $|f'| \simeq f_1$ and $|f-f'| \simeq f_2$ separately,

$$F(f) \simeq \int E_1(f_1)E_2(|f|) df' + \int E_1(|f|)E_2(f_2) df'. \quad (\text{A.3})$$

The two integrals on the right-hand side are $\propto |f|^{\alpha_4}$ and $\propto |f|^{\alpha_2}$, respectively, and therefore $F(f) \propto |f|^{\max(\alpha_2, \alpha_4)}$ when $|f|$ is sufficiently large.

In Fig. A.1 we demonstrate the idea by convolving two spectra with $(\alpha_1, \alpha_2, \alpha_3, \alpha_4) = (1, -3, 2, -4)$ and $(f_1, f_2) = (100, 200)$. The convolved spectrum $F(f)$ is flat at low frequencies and $\propto f^{-3}$ at high frequencies, as expected.

The above reasoning can be extended to the case where $\alpha_1 = 0$, e.g., E_1 might result from a prior convolution between two broken power-law spectra. The primary contributions to the convolution integral become (i) $|f'| \leq f_1$ and (ii) $|f-f'| \simeq f_2$, and the proof above can be similarly carried out. When applying these conclusions to the outcome of successive convolutions of several E_i terms, we observe that the resulting PSD will be flat at low frequencies and exhibit a slope corresponding to the shallowest α_2 of the convolved spectra.

References

- Arévalo, P., Churazov, E., Lira, P., et al. 2024, *A&A*, 684, A133
 Bai, X.-N. & Stone, J. M. 2013, *ApJ*, 767, 30
 Balbus, S. A. & Hawley, J. F. 1991, *ApJ*, 376, 214
 Bardeen, J. M. & Petterson, J. A. 1975, *ApJL*, 195, L65
 Beckwith, K., Hawley, J. F., & Krolik, J. H. 2009, *ApJ*, 707, 428
 Blackman, E. G. & Nauman, F. 2015, *Journal of Plasma Physics*, 81, 395810505
 Blackman, E. G., Penna, R. F., & Varnière, P. 2008, *New A*, 13, 244
 Bucciantini, N. & Del Zanna, L. 2013, *MNRAS*, 428, 71
 Bugli, M., Del Zanna, L., & Bucciantini, N. 2014, *MNRAS*, 440, L41
 Burke, C. J., Shen, Y., Blaes, O., et al. 2021, *Science*, 373, 789
 Cai, Z.-Y., Wang, J.-X., Gu, W.-M., et al. 2016, *ApJ*, 826, 7
 Cao, X. & Spruit, H. C. 2013, *ApJ*, 765, 149
 Chandrasekhar, S. 1961, *Hydrodynamic and hydromagnetic stability* (Courier Corporation)
 Chen, B.-Y., Bower, G. C., Dexter, J., et al. 2023, *ApJ*, 951, 93
 Cowperthwaite, P. S. & Reynolds, C. S. 2014, *ApJ*, 791, 126
 Dexter, J. & Agol, E. 2011, *ApJL*, 727, L24
 Dhang, P., Bendre, A., Sharma, P., & Subramanian, K. 2020, *MNRAS*, 494, 4854
 Dyda, S., Lovelace, R. V. E., Ustyugova, G. V., Koldoba, A. V., & Wasserman, I. 2018, *MNRAS*, 477, 127
 Fendt, C. & Gaßmann, D. 2018, *ApJ*, 855, 130
 Frank, J., King, A., & Raine, D. J. 2002, *Accretion Power in Astrophysics: Third Edition* (Cambridge university press)
 Gressel, O. 2010, *MNRAS*, 405, 41
 Guilet, J. & Ogilvie, G. I. 2012, *MNRAS*, 424, 2097
 Guilet, J. & Ogilvie, G. I. 2013, *MNRAS*, 430, 822
 Hagen, S., Done, C., & Edelson, R. 2024, *MNRAS*, 530, 4850
 Hogg, J. D. & Reynolds, C. S. 2016, *ApJ*, 826, 40
 Hogg, J. D. & Reynolds, C. S. 2018, *ApJ*, 861, 24
 Ingram, A. & van der Klis, M. 2013, *MNRAS*, 434, 1476
 Janiuk, A. & Czerny, B. 2007, *A&A*, 466, 793
 Kelly, B. C., Bechtold, J., & Siemiginowska, A. 2009, *ApJ*, 698, 895
 King, A. R., Pringle, J. E., West, R. G., & Livio, M. 2004, *MNRAS*, 348, 111
 Krolik, J. H., Horne, K., Kallman, T. R., et al. 1991, *ApJ*, 371, 541
 Liska, M., Tekehovskoy, A., & Quataert, E. 2020, *MNRAS*, 494, 3656
 Lyubarskii, Y. E. 1997, *MNRAS*, 292, 679
 MacLeod, C. L., Ivezić, Ž., Kochanek, C. S., et al. 2010, *ApJ*, 721, 1014
 Mayer, M. & Pringle, J. E. 2006, *MNRAS*, 368, 379
 Mushotzky, R. F., Edelson, R., Baumgartner, W., & Gandhi, P. 2011, *ApJL*, 743, L12
 Nelson, R. P. & Papaloizou, J. C. B. 2000, *MNRAS*, 315, 570
 Pei, L., Barth, A. J., Aldering, G. S., et al. 2014, *ApJ*, 795, 38
 Pencil Code Collaboration, Brandenburg, A., Johansen, A., et al. 2021, *The Journal of Open Source Software*, 6, 2807
 Ren, G., Zhou, S., Sun, M., & Xue, Y. 2024, arXiv e-prints, arXiv:2409.09637
 Scaringi, S., Maccarone, T. J., Kording, E., et al. 2015, *Science Advances*, 1, e1500686
 Secunda, A., Jiang, Y.-F., & Greene, J. E. 2024, *ApJL*, 965, L29
 Shakura, N. I. & Sunyaev, R. A. 1973, *A&A*, 24, 337
 Sądowski, A., Narayan, R., Tekehovskoy, A., et al. 2015, *MNRAS*, 447, 49
 Smith, K. L., Mushotzky, R. F., Boyd, P. T., et al. 2018, *ApJ*, 857, 141
 Stepanovs, D., Fendt, C., & Sheikhezami, S. 2014, *ApJ*, 796, 29
 Stone, Z., Shen, Y., Burke, C. J., et al. 2022, *MNRAS*, 514, 164
 Su, Z.-B., Cai, Z.-Y., Sun, M., et al. 2024, *ApJ*, 969, 78
 Sun, M., Xue, Y., Brandt, W. N., et al. 2020, *ApJ*, 891, 178
 Tang, J.-J., Wolf, C., & Tonry, J. 2023, *Nature Astronomy*, 7, 473
 Tomei, N., Del Zanna, L., Bugli, M., & Bucciantini, N. 2020, *MNRAS*, 491, 2346
 Turner, S. G. D. & Reynolds, C. S. 2021, *MNRAS*, 504, 469
 Uttley, P. & McHardy, I. M. 2001, *MNRAS*, 323, L26
 Uttley, P., McHardy, I. M., & Vaughan, S. 2005, *MNRAS*, 359, 345
 Velikhov, E. P. 1959, *Soviet Journal of Experimental and Theoretical Physics*, 9, 995
 von Rekowski, B., Brandenburg, A., Dobler, W., Dobler, W., & Shukurov, A. 2003, *A&A*, 398, 825
 Vourellis, C. & Fendt, C. 2021, *ApJ*, 911, 85
 Wang, Z. F., Burke, C. J., Liu, X., & Shen, Y. 2023, *MNRAS*, 521, 99
 Wolf, C., Lai, S., Tang, J. J., & Tonry, J. 2024, arXiv e-prints, arXiv:2411.02759
 Zhang, H., Yang, S., & Dai, B. 2024, *ApJL*, 967, L18
 Zhou, H. 2024, *MNRAS*, 527, 3018
 Zhou, S., Sun, M., Cai, Z.-Y., et al. 2024, *ApJ*, 966, 8
 Zu, Y., Kochanek, C. S., Kozłowski, S., & Udalski, A. 2013, *ApJ*, 765, 106